Eco-friendly synthesis of graphene oxide–palladium nanohybrids

Rodríguez-Otamendi, Dinorah I.; Bizarro, Monserrat; Meza-Laguna, Víctor; Álvarez-Zauco, Edgar; Rudolf, Petra; Basiuk, Vladimir A.; Basiuk, Elena V.

Published in:
Materials today communications

DOI:
10.1016/j.mtcomm.2023.106007

Publication date:
2023

Materials Today Communications 35 (2023) 106007

Contents lists available at ScienceDirect

Materials Today Communications

journal homepage: www.elsevier.com/locate/mtcomm

Eco-friendly synthesis of graphene oxide–palladium nanohybrids

Dinorah I. Rodríguez-Otamendi [a,b,*,1], Monserrat Bizarro [c,2], Víctor Meza-Laguna [d,3], Edgar Álvarez-Zauco [e,4], Petra Rudolf [b,5], Vladimir A. Basiuk [d,6], Elena V. Basiuk [a,**,7]

[a] Instituto de Ciencias Aplicadas y Tecnología, Universidad Nacional Autónoma de México, Circuito Exterior C.U., 04510 Cd. México, Mexico
[b] Zernike Institute for Advanced Materials, University of Groningen, Nijenborgh 4, 9747 AG Groningen, the Netherlands
[c] Instituto de Investigaciones en Materiales, Universidad Nacional Autónoma de México, Circuito Exterior C.U., 04510 Cd. México, Mexico
[d] Instituto de Ciencias Nucleares, Universidad Nacional Autónoma de México, Circuito Exterior C.U., 04510 Cd. México, Mexico
[e] Facultad de Ciencias, Universidad Nacional Autónoma de México, Circuito Exterior C.U., 04510 Cd. México, Mexico

ARTICLE INFO

Keywords:
Graphene oxide
Palladium nanoparticles
Nanohybrids
Solvent-free functionalization
Eco-friendly approach
Characterization

ABSTRACT

Nanostructured hybrids of graphene oxide and palladium were fabricated by means of one-step solvent-free gas phase treatment of graphene oxide with the aliphatic amines 1-octadecylamine and 1,8-diaminooctane, followed by *in situ* decoration with palladium in the liquid medium using palladium chloride as the precursor and citric acid as a mild and environmentally friendly stabilizing and reducing agent. The proposed synthesis method represents an eco-friendly alternative for obtaining nanohybrids of graphene oxide and palladium nanoparticles under mild conditions. Spectroscopic studies evidenced -COOH group derivatization of graphene due to the amidation reaction; transmission electron microscopy demonstrated the formation of nanometer-sized crystalline palladium particles and evidenced that the diamine-functionalization results in a larger particle sizes than observed for monoamine- or non-functionalized substrates. The hybrids obtained have a slightly lower thermal stability than pristine graphene oxide.

1. Introduction

In recent years graphene oxide (GO) has emerged as a highly promising material for applications in energy storage (batteries and supercapacitors), catalysis [1–4], sensors, as well as building block of conducting and thermal materials, filtration membranes and bactericidal agents [5–9]. Combining the properties of metal nanoparticles with those of GO through covalent assembly results hybrid architectures offer additional technological possibilities [10–18] due to their large surface area, plasmon resonance, highly stable nature, and in general easy processing [19–21]. It has been demonstrated that amino groups, along with the oxygen-containing groups already present in GO [22], act as nucleation points for metal nanoparticles that form through coordination bonds or electrostatic interactions with metal ions [23–26]. One of the simplest methods for metal nanoparticle deposition is liquid phase chemical reduction of the respective salts with the help of stabilizing and dispersing agents, which help to avoid agglomeration and therefore control size and morphology [11–19], favouring the uniform distribution of nanoparticles on the GO surface [27].

In our previous work [28], we demonstrated that the formation of nanostructured hybrid materials employing amine-functionalized GO to support silver nanoparticles (AgNPs) can be achieved *via* a simple and eco-friendly gas-phase treatment. We have shown that this method of synthesis does not require additional purification processes because the

* Corresponding author at: Instituto de Ciencias Aplicadas y Tecnología, Universidad Nacional Autónoma de México, Circuito Exterior C.U., 04510 Cd. México, Mexico.
** Corresponding author.
E-mail addresses: d.i.rodriguez.otamendi@rug.nl (D.I. Rodríguez-Otamendi), elena.golovataya@icat.unam.mx (E.V. Basiuk).
[1] 0000-0001-5495-6081
[2] 0000-0002-4716-9730
[3] 0000-0002-7812-6231
[4] 0000-0003-2560-5906
[5] 0000-0002-4418-1769
[6] 0000-0001-7864-9203
[7] 0000-0003-0877-242X

https://doi.org/10.1016/j.mtcomm.2023.106007
Received 10 April 2023; Accepted 13 April 2023
Available online 21 April 2023

surplus reagents can be eliminated *in situ* through moderate dynamic vacuum and heating conditions. With respect to conventional techniques where toxic solvents are employed and several reaction steps are involved [29,30], the one-step gas-phase amine functionalization method has the advantage of yielding AgNPs with a controlled size distribution and a higher surface density, which are important requirements for applications of GO hybrid materials in several fields [31–34]. This motivates a further study on other noble metals like palladium in view of exploiting not only the peculiar electronic, mechanical, and catalytic properties of these nanoparticles, [35–37] but also their application for therapeutic purposes based on their antibacterial and cytotoxic activity [38–40].

The main purpose of the present work was to demonstrate that it is possible under eco-friendly and mild conditions to obtain nanohybrids of GO and palladium nanoparticles (PdNPs) by applying a gas-phase pretreatment of GO with amine molecules, which thanks to their chemical affinity toward biological molecules [41], confer an additional ecological value to this study. Similar studies with pristine, non-functionalized materials will be performed as well for comparison purposes.

2. Experimental

2.1. Materials

Single-layer graphene oxide powder (≥99 wt% purity, platelet diameter of 300–800 nm and thickness of 0.7–1.2 nm) from Cheap Tube, Inc., was used. 1-Octadecylamine (ODA; ≥99%), 1,8-diaminooctane (DAO; ≥98%), citric acid (≥99.5%), palladium chloride (≥99%), 2-propanol (≥99.8%) and hydrochloric acid (≥37%) from Sigma-Aldrich were used as received.

2.2. Gas phase functionalization with amines

We followed the general procedure described in our previous works [42–44] and optimized it for the present purposes. The yield was improved employing GO/amine w/w ratios of 1:1. The functionalization process comprised three steps: (1) degassing for 15 min at temperature of 100 °C under constant evacuation pressure of 10^{-2} Torr; (2) functionalization reaction under static vacuum for 1 h in a temperature range of 160–180 °C; (3) degassing at 100 °C under constant evacuation for 30 min to remove unreacted amines.

The amine-functionalized samples are labelled GO+ODA and GO+DAO in the following.

2.3. Deposition of palladium nanoparticles

We adapted the methods of PdNP deposition based on the reduction of Pd^{2+} ions with citric acid, reported by Roy et al. [45], Dar et al. [46], and Li et al. [47]. Compared to Dar et al. [46], we reduced the reaction time from 7 h to 10 min by adopting the acidic solution of $PdCl_2$ employed by Li et al. [47] and, in order to assure the complete reduction reaction of the precursor, the citric acid concentration was 10 times higher. For achieving homogeneous dispersions, it was necessary to dissolve the metallic precursor in a 0.2 N solution of HCl assisted by heating at about 70 °C, which was then diluted with distilled water to obtain $PdCl_2$ 0.005 M.

For preparing the hybrids, amine-functionalized and pristine GO were immersed in 0.005 M $PdCl_2$ in a proportion of 5 mg/10 mL. Then, 20 mL of a 0.05 M solution of citric acid was added to the reaction vessel upon continuous stirring at room temperature for 10 min. After this, the materials were washed twice with deionized water, dried, and stored under vacuum at room temperature. The amine-functionalized samples decorated with PdNPs are labelled GO+ODA+Pd and GO+DAO+Pd in the following. An analogous sample was obtained with non-functionalized pristine GO for comparison. This hybrid is labelled GO+Pd in the following.

2.4. Characterization

Fourier-transform infrared (FTIR) spectra in attenuated total reflectance (ATR) mode were measured employing a Nicolet iS50R Thermo-Scientific spectrometer. Each spectrum was the sum of 32 scans, collected in the range of 500–4000 cm^{-1} with a resolution of 4 cm^{-1}. Measurements were performed in triplicate to verify reproducibility.

The X-ray powder diffraction (XRD) data were obtained on a D8 Advance Bruker diffractometer with a monochromatic Cu Kα X-ray source (λ = 1.5418 Å) and a secondary beam graphite monochromator; a LYNXEYE detector (1D mode) was used. The samples were finely pulverized and the patterns were recorded in a 2θ range from 3° to 60°, in steps of 0.02° and with a counting time of 1.0 s per step; duplicate spectra were acquired.

Thermogravimetric and differential thermal analysis (TGA–DTA) were carried out using a STA 449 C Jupiter analyzer from Netzsch-Geratebau GmbH. For the tests, samples of approximately 10 mg were exposed to an air flow of 100 mL/min, and a heating ramp of 10 °C/min up to 1000 °C; duplicate analysis was performed.

Scanning electron microscopy (SEM) was performed with a JEOL JSM-6510LV instrument, operated at an acceleration voltage of 20 kV, and coupled to an INCA Energy 250 Energy Dispersive X-ray (EDS) Microanalysis System from Oxford Instruments. All the samples were fixed on double-sided carbon tape and measured without coating. Two imaging modes were used: secondary electrons images (SEI) and back-scattered electron composition (BEC), collecting micrographs at 10, 5 and 0.5 μm. SEM-EDS spectra were acquired for every sample in 5 different spots with a diameter of 30 μm.

Transmission electron microscopy (TEM) bright-field (BF) and dark-field (DF) studies were carried out with a JEOL JEM-ARM200F STEM Schottky FEG, operated at a 1.0 Å resolution and a 200 kV acceleration voltage. The samples were dispersed in 2-propanol, drop casted onto lacey carbon films on 200 mesh copper TEM grids manufactured by Agar Scientific, dried at room temperature and cleaned by plasma treatment before measurements. Micrographs at 200, 100 and 20 nm were performed in BF mode, whereas DF imaging at 0.5 μm, 100 and 20 nm were collected from different spots on every sample. TEM-EDS mapping was performed for every sample on 3 different spots with a diameter of 1 μm.

2.5. Theoretical calculations

To gain theoretical insight into the mechanisms of interaction of PdNPs with pristine and amine-functionalized GO as well as into the geometry and formation energies of the resulting Pd-GO hybrids, we employed density functional theory (DFT) calculations. The numerical-based DFT module $DMol^3$ [48–51] of Materials Studio was the software package of choice. We used the Perdew-Burke-Ernzerhof (PBE) functional [52] within the generalized gradient approximation, along with a long-range dispersion correction by Grimme [53] (commonly referred to as PBE-D2), which is crucial when noncovalent interactions are involved. The double numerical basis set DNP, which has a polarization *d*-function added on all non-hydrogen atoms, as well as a polarization *p*-function added on all H atoms, was combined with the DSPP pseudopotentials. The settings for full geometry optimization and calculation of electronic parameters included 'fine' computation quality and convergence criteria (namely, 10^5 Ha energy change, 0.002 Ha/Å maximum force, 0.005 Å maximum displacement, and 10^{-6} SCF tolerance). All the calculations were spin-unrestricted. The global orbital cutoff [54] was set to 4.5 Å, as defined by the presence of palladium atoms. Since setting orbital occupancy to Fermi-type not always allowed for the reasonably fast and successful SCF convergence, for the most complex systems the latter was aided by using thermal smearing [54–56], the value of which was reduced stepwise from 0.005 to 10^{-4} Ha, and the final calculation was refined with Fermi orbital occupancy

(with a few exceptions).

All the calculations considered the presence of an aqueous medium, whose implicit inclusion was performed *via* the conductor-like screening model (COSMO) [57,58] with the value of 78.54 for dielectric constant of water.

The formation energies $\Delta E_{GOmodel+PdNC}$ for the complexes (or ΔE for simplicity) of different GO models (GOmodel) with a palladium nanocluster (PdNC) were calculated using the following general equation:

$$\Delta E_{GOmodel+PdNC} = E_{GOmodel+PdNC} - (E_{GOmodel} + E_{PdNC})$$

where E_i is the corresponding absolute energy.

3. Results and discussion

3.1. Experimental results

To visualize general changes in the chemical nature of GO before and after functionalization with amines and further decoration with PdNPs, dispersibility tests were conducted in water and 2-propanol. For this purpose, 0.5 mg/mL dispersions of GO in solvent were prepared with ultrasonication for 10 min at room temperature (Fig. 1). For pristine GO, brownish dispersions were formed in both water and 2-propanol, which precipitated after 24 h. Amine-functionalized GO formed instable dispersions in water, whereas in 2-propanol the stability of the dispersions deceased with time and almost total precipitation was observed after 24 h. These results confirm that the surfaces modified with long chains of ODA and DAO acquire a more hydrophobic character. Once decorated with PdNPs, the amine-functionalized GO solids precipitated to the bottom of the beakers in both solvents practically immediately after sonication.

The effectiveness of amine derivatization *via* GO surface chemistry was checked with the help of FTIR spectroscopy (Fig. 2). The spectrum of pristine GO shows the fingerprint bands of the oxygen-containing moieties: the hydroxyl band (ν_{OH}) at 3592 cm^{-1}; the δ_{OH} signal at 1607 cm^{-1}; $\nu_{C=O}$ vibrations in COOH groups at 1719 cm^{-1}; $\nu_{C\text{-}O(asym)}$ in epoxy bonds [59] at 1373 cm^{-1}; the δ_{OH} signal at 1241 cm^{-1} and the $\nu_{C\text{-}O}$ vibrations at 1051 cm^{-1} from C–O–H groups [60]. Unsaturated ketone groups could be responsible for the band at 964 cm^{-1} [43]. For aminated GO the $\nu_{C=O}$ signal decreased in intensity and shifted, from 1704 to 1719 cm^{-1} to 1694–1699 cm^{-1}, due to the characteristic 'amide I' band between 1600 and 1700 cm^{-1}, accompanied by the 'amide II' band at 1558–1563 cm^{-1} [22,61,62]. The set of bands located at 1200–1400 cm^{-1} can be assigned to the 'amide III' mode [61,62]. Additionally, the bands of alkyl groups are observed: the $\nu_{CH(asym)}$ band at 2916–2921 cm^{-1} and the $\nu_{CH(sym)}$ band at 2843–2848 cm^{-1}. These observations corroborate a successful amine derivatization.

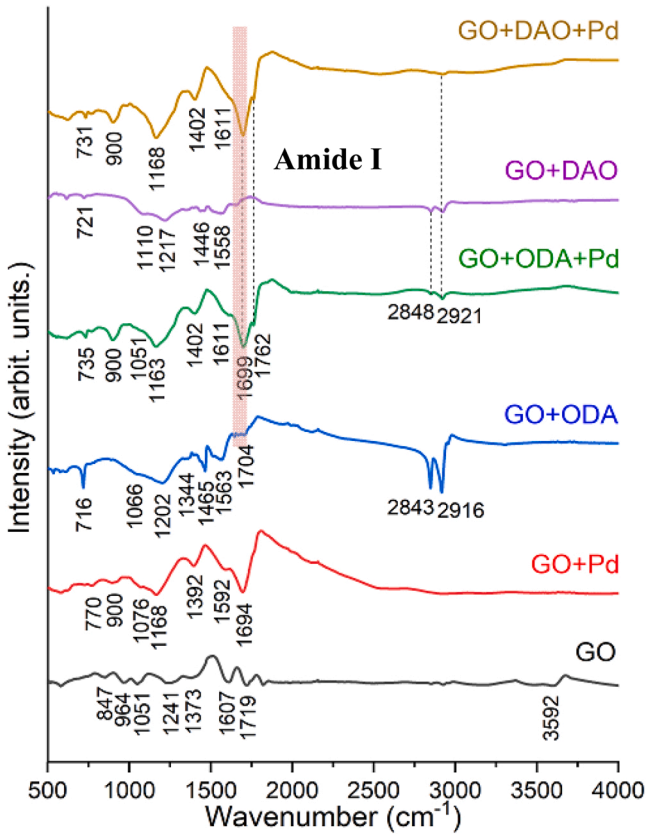

Fig. 2. FTIR spectra of pristine and amine-functionalized GO samples before and after decoration with Pd nanoparticles.

For GO-Pd samples, clear changes can be observed in the bands corresponding to the vibrations of the oxygenated groups; in particular, the increased intensity, broadening and shifting of $\nu_{C=O}$ absorption band

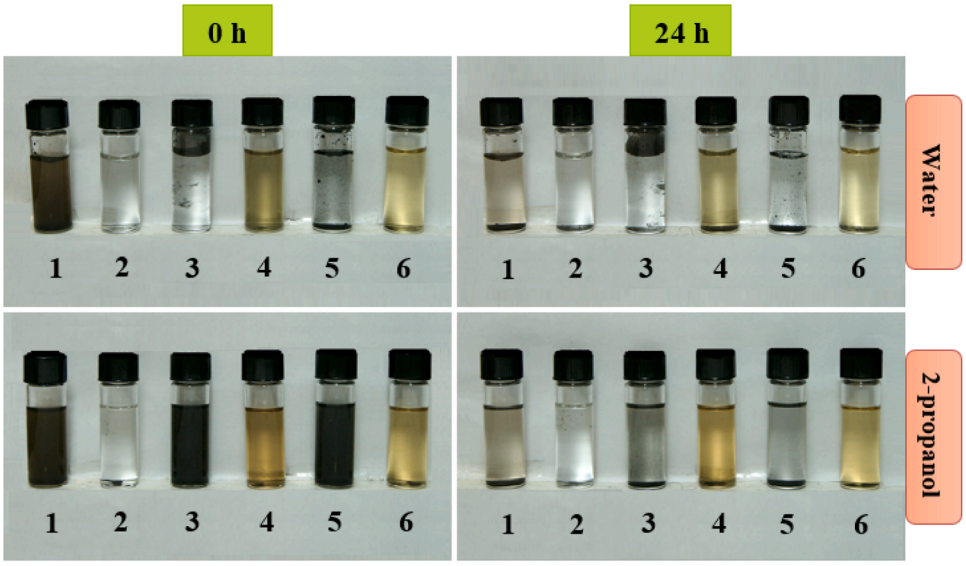

Fig. 1. Dispersibility tests for GO samples in water and 2-propanol: (1) pristine GO, (2) GO+Pd, (3) GO+ODA, (4) GO+ODA+Pd, (5) GO+DAO, and (6) GO+DAO+Pd. The images were taken immediately after 10-min ultrasonication (0 h) and after 24 h.

from COOH functionalities might indicate that the palladium nanoparticles form a coordination bond with the oxygen in these groups. GO+ODA+Pd and GO+DAO+Pd samples show the same trend. Other important changes for these samples include an almost total disappearance of 'amide II' δ_{NH} absorption at 1558–1563 cm^{-1}, a decrease of the $\nu_{C\text{-}O}$ band at 1051–1076 cm^{-1} and an increase in intensity of $\nu_{C\text{-}N}$ signals at 1163–1168 cm^{-1}. All these changes indicate the coordination of palladium to nitrogen and oxygen atoms present on GO+ODA and GO+DAO surfaces.

TGA and DTA were used to identify changes in the thermal behaviour of GO caused by the modification with amines and the decoration with PdNPs. The TGA curve for pristine GO (Fig. 3a) exhibits three principal weight losses that correspond to the evaporation of physisorbed water (10.3%, until 136 °C), the pyrolysis of oxygenated functionalities (28.4%, until 245 °C), and the graphene lattice combustion (60.6%, until 690 °C) [63]. The DTA curve consists of two principal peaks in 211 and 668 °C, matching the main weight loss steps in the TGA curve.

For GO+Pd (Fig. 3b), the pattern of weight loss includes four steps. The first is related to the evaporation of physisorbed water (5.6%, until 134 °C), the second refers to the pyrolysis of oxygenated groups (37.8%, until 247 °C), the third one is related to the combustion of the main graphene backbone (45.1%, until 446 °C), and the fourth weight loss (6.4%, until 797 °C) can be attributed to a portion of the palladium present in the sample. In fact, at temperatures over 420 °C, Pd slowly oxidizes to PdO_2 [64] and PdO_2 decomposes to Pd at temperatures above 780 °C. The last ramp (1.2%, until 1000 °C) mirrors the metallic Pd content. So, the total palladium content in the sample is around 11.5%. The DTA peaks refer to the combustion of the main components in the system, namely the oxygen-containing groups (239 °C), the graphene lattice (419 °C and 478 °C), and the palladium oxide (shoulder at 830 °C). The second and the third peak are strongly shifted to lower temperatures in comparison to the pristine GO sample; this can be explained by the catalytic effect of palladium on the combustion of the graphene backbone, similarly to what we saw previously for GO hybrids with silver nanoparticles [28].

For both amine-functionalized samples (Fig. 3c,d), the same percentage of 3.9% for the loss of physisorbed water was observed when heating up GO+ODA+Pd to 141 °C and GO+DAO+Pd to 138 °C. However, the loss steps for the oxygenated groups present noticeable differences; while for GO+ODA+Pd the corresponding percentage is 15.9% and the weight loss extends up to 247 °C, for GO+DAO+Pd the percentage is almost double, 29.5%, and the weight loss extends up to 293 °C. In the case of GO+ODA+Pd the main weight loss corresponds to the combustion of graphene lattice, 73.6% of the sample were lost when heating up to 500 °C, while for GO+DAO+Pd the weight loss is somewhat smaller, 63.9% and the temperature range slightly wider (heating up to 506 °C). Similarly to GO+Pd, these weight losses occur at lower temperatures compared to pristine GO, due to an apparent catalytic effect of the metal. Both thermograms show a shoulder at 828 °C, related to the decomposition of palladium oxide, which can be estimated to

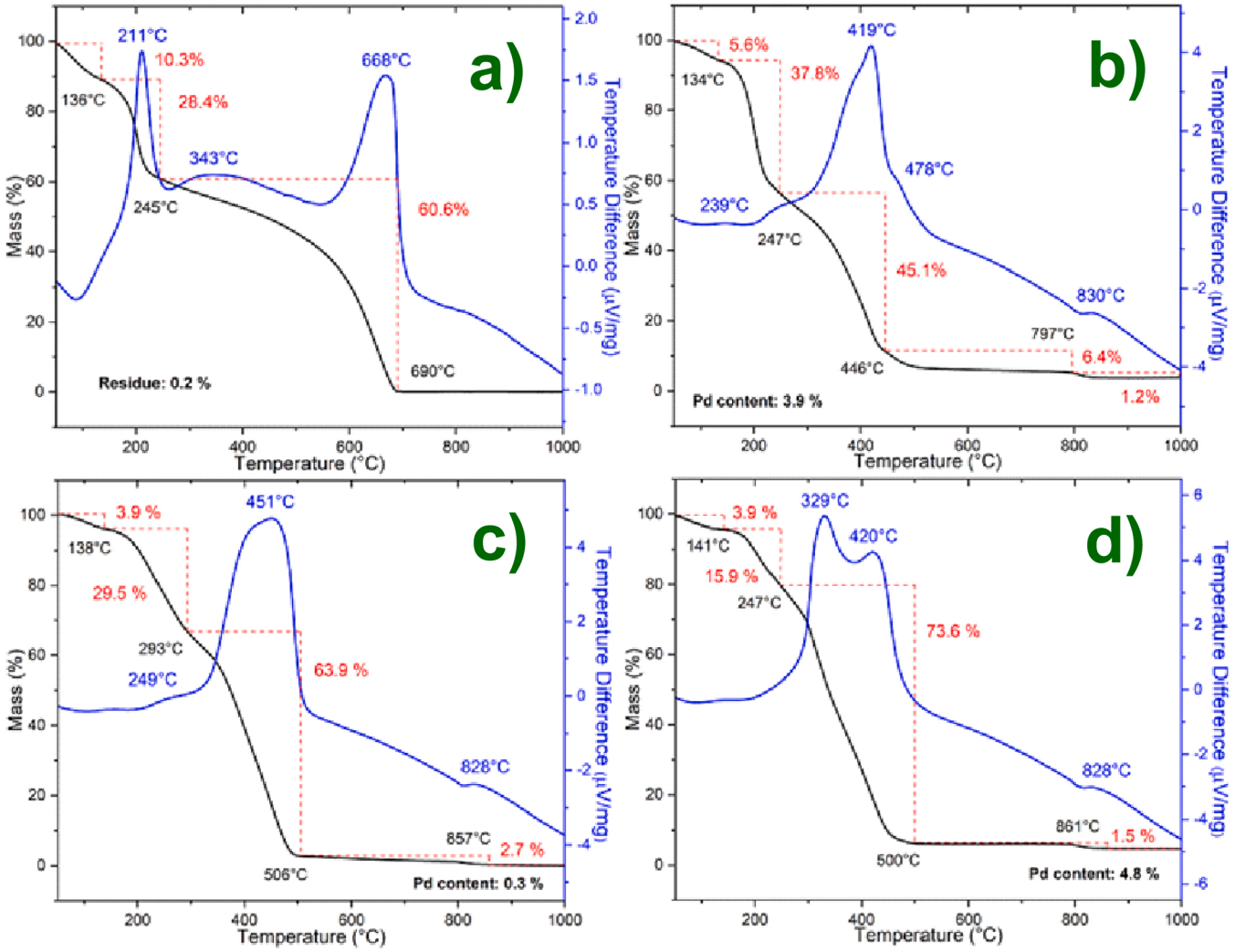

Fig. 3. TGA (black) and DTA (blue) curves for GO and GO hybrids: a) pristine GO, b) GO+Pd, c) GO+ODA+Pd, and d) GO+DAO+Pd.

make up 2.7% of GO+ODA+Pd, and 1.5% of GO+DAO+Pd. The metallic Pd content in every case is 0.3% for GO+ODA+Pd, and 4.8% for GO+DAO+Pd.

When comparing the TGA-DTA results for the GO+Pd series with those previously reported for the GO+Ag homologues [28], one notices that palladium importantly impacts the combustion temperature of the graphitic backbone; whereas for GO+Ag the pyrolysis starts at 682 °C, for GO+Pd it commences already at 446 °C. In the case of aminated samples, GO+ODA+Ag pyrolysis starts at 695 °C, but for GO+ODA+Pd it begins already at 506 °C, likewise for GO+DAO+Ag the combustion temperature is 716 °C, while for GO+DAO+Pd it is 500 °C. This testifies to a stronger catalytic effect of palladium nanoparticles. Another important difference concerns the final weight loss in the temperature range from 797° to 861°C in all the palladium-containing samples and corresponding to thermal decomposition of palladium oxide; this trend is not observed in the silver-containing hybrids because silver does not oxidize. Another difference is related to the final residue. While in the non-aminated GO hybrids the metal content is higher for palladium (GO+Pd: 11.5%; GO+Ag: 1.5%), in aminated samples one sees an opposite trend, namely a metal content of 3.0% for GO+ODA+Pd and of 6.3% for GO+DAO+Pd, while for GO+ODA+Ag the silver content amounts to 6.7% and for GO+DAO+Ag even to 12.1%.

To characterize the difference in chemical composition of the samples due to the functionalization with amines and further decoration with palladium particles, BEC SEM images were acquired (Fig. 4). The respective particle size distributions are presented in Fig. 5, where an asymmetrical distribution of size is clearly observed in all GO+Pd, GO+ODA+Pd and GO+DAO+Pd samples and small particle sizes dominate. The brightest spots highlight the presence of palladium particle agglomerates. For GO+Pd (Fig. 4a-c) triangular and octahedral shapes [65,66] with a narrow size distribution ranging from 0.04 to 0.34 μm and an average of 0.13 μm (Fig. 5a) are observed. The micrographs for GO+ODA+Pd (Fig. 4d–f), show mostly spherical palladium clusters in a broader range (0.03–1.2 μm) with an average particle size of about 0.26 μm (Fig. 5b). Similarly to the case of GO+Pd, also for GO+DAO+Pd (Fig. 4g–i) different geometric shapes are seen, from 0.02 to 0.85 μm, and the average particle size amounts to 0.14 μm (Fig. 5c). Comparing the particle size distributions, one notices that those for GO+Pd and GO+DAO+Pd are narrower than that of the ODA-functionalized sample. These observations agree with E. Ramirez et al. [67], who have demonstrated the predominant role of chemical equilibria between all potential coordinating agents in stabilizing the nanoparticles; here this concerns the ligands resulting from the precursor, the amine and the reducing agent. Since the mEq of ODA are lower than for DAO, for lower amine content we found aggregated particles but with a more regular shape. The size and shape of particles are governed by the nature of the stabilizing ligands and, in the case of weak ligands such as amines, by the quantity of ligand added.

The EDS results presented in Table 1 demonstrate that the metal content is highest for GO+Pd (10.0 ± 5.2 wt%; 1.4 ± 0.8 at%), followed

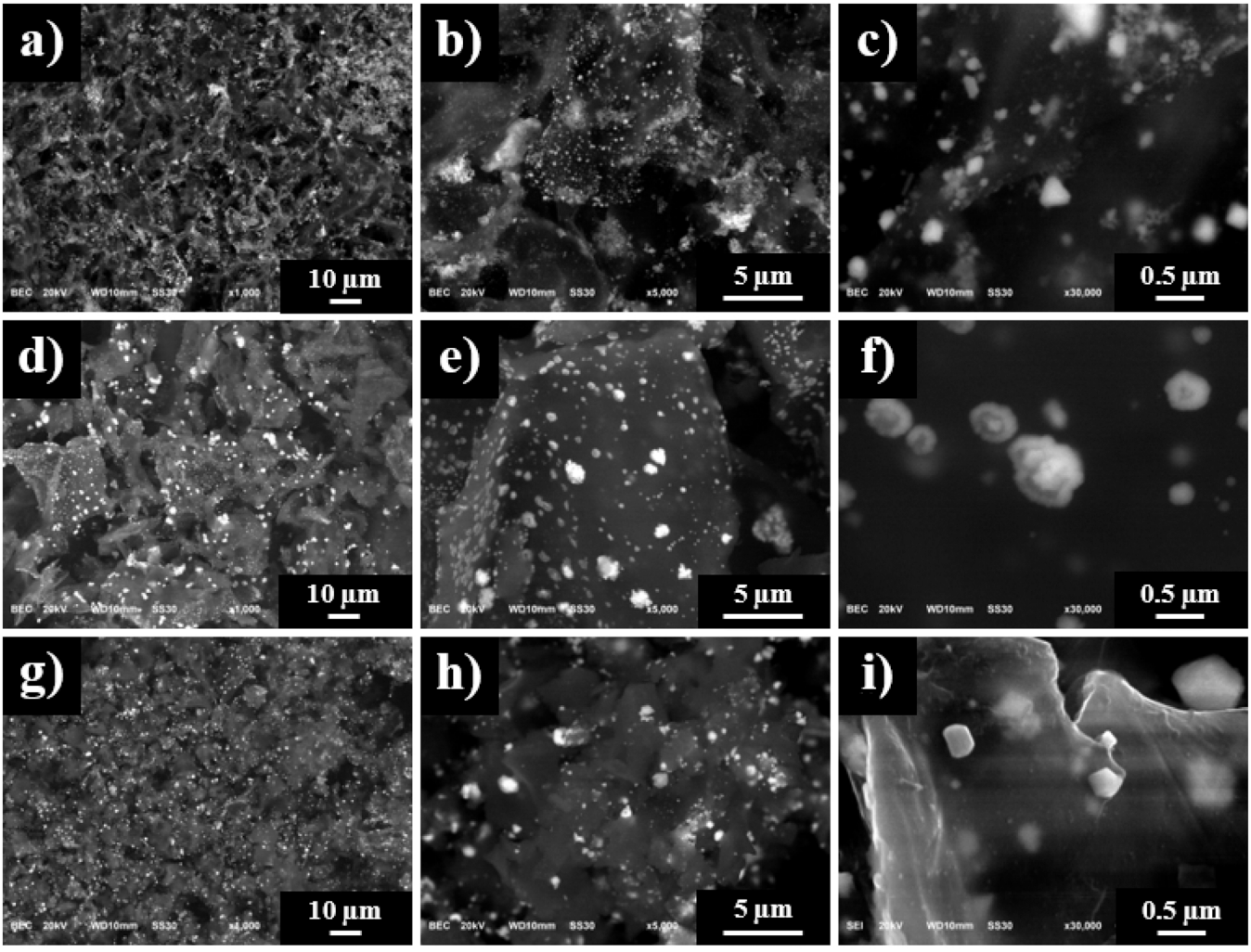

Fig. 4. Representative SEM images for GO+Pd (a-c), GO+ODA+Pd (d–f), and GO+DAO+Pd (g–i) at different magnification. Scale bars: 10 μm (left column); 5 μm (middle column), and 0.5 μm (right column).

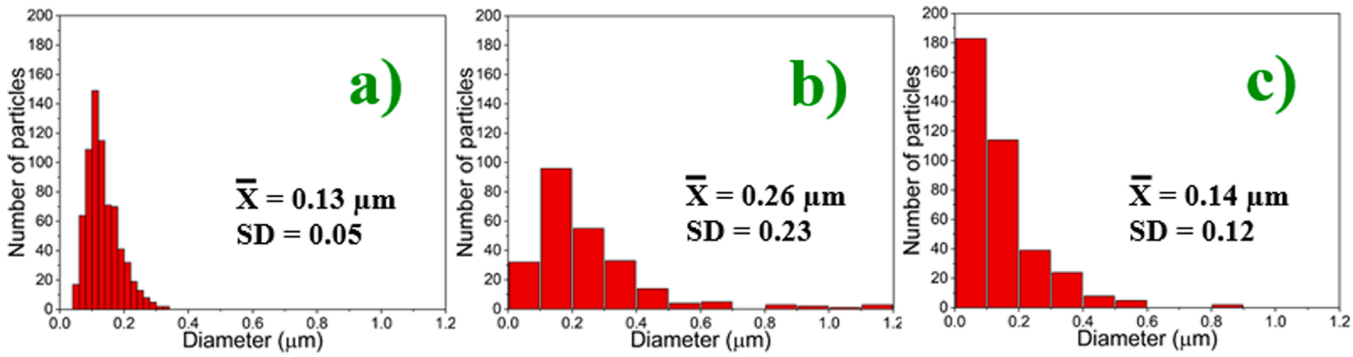

Fig. 5. Particle size distribution histograms obtained from SEM imaging of (a) GO+Pd, (b) GO+ODA+Pd and (c) GO+DAO+Pd.

Table 1
EDS results for the GO/PdNP series (SEM imaging).

Sample	Weight %	Atomic %
GO+Pd	C (K): 56.4 ± 8.8	C (K): 67.8 ± 6.3
	O (K): 33.6 ± 4.3	O (K): 30.8 ± 5.6
	Pd (L): 10.0 ± 5.2	Pd (L): 1.4 ± 0.8
GO+ODA+Pd	C (K): 62.9 ± 0.4	C (K): 70.7 ± 0.5
	O (K): 34.0 ± 0.7	O (K): 28.7 ± 0.5
	Pd (L): 2.5 ± 0.4	Pd (L): 0.3 ± 0.04
GO+DAO+Pd	C (K): 58.7 ± 6.3	C (K): 68.9 ± 4.4
	O (K): 33.6 ± 3.4	O (K): 29.8 ± 4.0
	Pd (L): 6.9 ± 4.1	Pd (L): 0.9 ± 0.6

by GO+DAO+Pd (6.9 ± 4.1 wt%; 0.9 ± 0.6 at%), and GO+ODA+Pd (2.5 ± 0.4 wt%; 0.3 ± 0.04 at%). Despite the differences in particle size, the tendencies observed in Fig. 5 match those of the thermal studies.

To also study the morphology, size, and distribution of smaller GO-supported palladium particles we collected bright-field (Fig. 6) and dark-field (Fig. 7) TEM micrographs. The corresponding particle size histograms are presented in Fig. 8. For GO+Pd (Figs. 6 and 7a-c) strong agglomeration of differently shaped metallic particles can be observed, leading to a broad size distribution ranging from 2 to 15 nm, and an average particle size of 5.7 ± 2.3 nm (Fig. 8a). On ODA-functionalized GO, spherical particles ranging from 1 to 13 nm are observed, with an average size of 4.2 ± 1.4 nm (Fig. 8b), whereas on DAO-functionalized GO, the particles are much larger, ranging from 6 to 450 nm, and the average size is 52.5 ± 83.5 nm (Fig. 8c).

TEM EDS mapping (Fig. 9) was carried out to supplement the micrographs with results on the chemical composition. The highest Pd content was found for the hybrid with pristine GO, followed by that for DAO-functionalized GO, and finally by that for ODA-functionalized GO. According to the elemental maps, the most homogeneous distribution with minimal agglomeration can be observed for GO+ODA+Pd, while GO+Pd and GO+DAO+Pd show a strong coalescence of particles. These results are not as informative on the average composition of the hybrids as the SEM EDS results because they represent a snapshot on the local composition of a much smaller area (TEM spot diameter 1 µm *vs.* SEM spot diameter 30 µm) but they match the trend in Pd content previously discussed in SEM EDS, and agree with the thermal behaviour of the hybrids.

The agglomeration observed in the non-aminated sample can be associated with the strong interaction of sterically unprotected Pd species with the GO surface. The smallest particle size achieved in GO+ODA+Pd can be justified by the presence of the ODA moieties, which avoid a strong attraction to the graphitic backbone. In GO+DAO+Pd, the two coordinating sites of DAO favour a higher content of metallic nanoparticles, which is mirrored by the histograms in Figs. 5 and 8, and the percentage of Pd observed in EDS studies (Tables 1 and 2).

Compared with Ag-containing samples, larger particles with a broader size distribution were observed in the GO+Pd series, despite a slightly lower palladium content. It is important to highlight a strong tendency of agglomeration of either silver or palladium nanoparticles on pristine graphene oxide, which underlines the importance of nitrogen-containing ligands for nucleation and growth regulation [67].

The crystallinity of the Pd-containing hybrids was investigated by XRD and the diffractograms acquired are shown in Fig. 10. GO presents the characteristic (001) diffraction peak at $2\theta = 11.2°$ (*d*-spacing of 0.79 ± 0.007 nm) [68–71]. In fact, according to Dékány, Krüger--Grasser, and Weiss [72], pristine GO presents *d*-spacings between 0.61 up to 1.1 nm, depending on the amount of water adsorbed. The modification with amines resulted in a broadening of the main GO peak and a shifting from 11.2° to 11.7° ($d_{001} = 0.76 \pm 0.007$ nm) for GO+ODA, and to 12.5° ($d_{001} = 0.71 \pm 0.009$ nm) for GO+DAO. This slight shrinking of the interlamellar space could be associated with the hydrophobic aliphatic chain of the amine moieties. For GO+Pd, GO+ODA+Pd and GO+DAO+Pd hybrids a noticeable broadening of the graphitic peak at $2\theta = 13.4°$ (*d*-spacing of 0.66 nm) is seen; this points to small coherently diffracting domains and hence to (partial) exfoliation [73]. According to Kaniyoor et al., this phenomenon might be provoked by the acid treatment preparing for the decoration with PdNPs; in fact a partial removal of oxygenated functionalities (a certain degree of reduction) and water molecules, decreases the interlayer spacing in comparison to pristine GO [74–77]. FT-IR and TGA/DTA results support this interpretation. It is reasonable to assume that the acidic treatment of aminated-GO also has an impact on the flake thickness *via* exfoliation-reduction [73], which causes the broad (001) Bragg reflection peak. The exfoliatiation seems to continue during Pd decoration since for both GO+ODA+Pd and GO+DAO+Pd hybrids the 001 peak has almost totally disappeared, indicating that the coherently diffracting domains are very small. The slightly narrower *d*-spacing for GO+DAO is probably due to cross-linking by bifunctional molecules like 1,8 diamino octane onto the GO network, resulting in a more compact hybrid [44,78].

The appearance of new peaks assigned to (111) and (200) Bragg reflections at $2\theta = 40.2°$ and 46.7° respectively, in the Pd-containing hybrids confirmed that the palladium nanoparticles that are large enough to be detected in XRD, have a face centred cubic (fcc) crystalline structure [79]. The fact that the intensity of the peaks in aminated samples is higher than in the non-aminated GO+Pd indicates more periodicity in crystalline arrangements due to the complexation effect by the nitrogen in amines. The lack of these stabilizing agents on the chemical environment of GO+Pd promotes chaotic/random arrangements; as a consequence, the height of the peak is reduced. These phenomena match the discussion of the SEM and TEM images (*vide supra*) where we saw that ligand moieties have an impact on the nucleation patterns of metallic particles.

3.2. *Theoretical modeling*

We attempted to provide an explanation for the experimental results

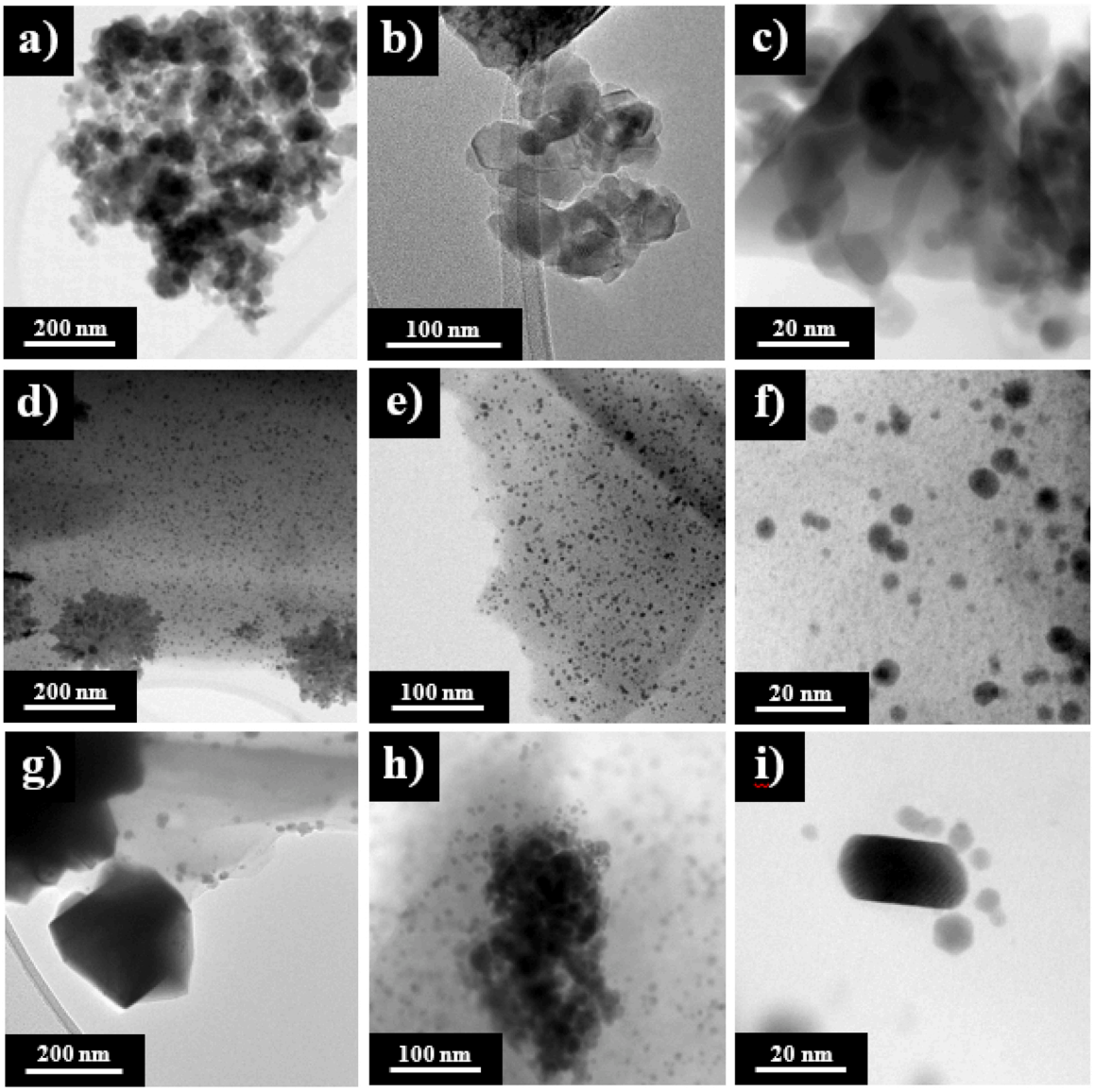

Fig. 6. Bright-field TEM imaging for GO+Pd (a-c), GO+ODA+Pd (d-f) and GO+DAO+Pd (g-i) at different magnification. Scale bars: 200 nm (left column); 100 nm (middle column), and 20 nm (right column).

by modeling the properties of the hybrids with DFT calculations. The use of realistic-size GO and PdNP models is obviously computationally prohibitive, but relatively small models can already highlight some trends. An appropriate and computationally accessible choice to simulate a Pd nanoparticle is the Pd_{16} cluster (Fig. 11), which was proposed by Nava et al. [80]. This cluster has a maximal lateral extension of 7.1 Å and can also be synthesized experimentally in a ligand-stabilized form [81]. In the case of GO, we employed the models of pristine GO, GO+ODA and GO-DAO successfully tested in our previous study on AgNP decoration of the same substrates [28].

The optimized Pd_{16} geometry (Fig. 11a) is rather symmetric. As shown by the Mulliken analysis, the atoms of the cluster differ in terms of the sign and magnitude of charge: from − 0.041 *e* to 0.013 *e*. In other words, both positively and negatively charged chemical species (either atoms or functional groups) can interact electrostatically with Pd_{16} and this will be important for how the metal nanoparticles can bind to pristine and functionalized GO.

As described previously [28], a computationally feasible choice of GO models is based on a ten fused aromatic-ring system [82,83]. To represent the oxygen-containing functionalities of GO, we introduced six carboxylic and eight aromatic ketone groups. The models for GO+ODA and GO+DAO were derived from the GO model by converting four of its six COOH groups into the corresponding amides [28]. In the case of GO+DAO we additionally accounted for the fact that the Pd deposition is carried out under acidic experimental conditions, by protonating the four NH_2 termini, which did not form amide derivatives; the resulting model is referred to as GO+DAO-4 H^+.

The DFT results related to complex formation and the frontier orbital energies are presented in Table 3. Fig. 12. schematically describes the mechanism and energy of complexation of a Pd_{16} cluster with the models for pristine GO, GO+ODA and GO+DAO-4 H^+. One can see that the weakest bonding (−62.2 kcal/mol) was found on GO+ODA. In this case, Pd_{16} remains on the top of the model, forming close contacts mainly with the terminal CH_3 groups of octadecyl moieties. The other two cases are very different, with very low negative values of formation energies (*i.e.* very strong bonding) for both GO (−135.2 kcal/mol) and especially GO+DAO-4 H^+ (−179.5 kcal/mol). The most interesting distinctive feature is that the Pd cluster directly chemisorbs on the graphene backbone by forming short Pd-C bonds, which can be qualified as covalent. This happens even on GO+DAO-4 H^+, despite the presence

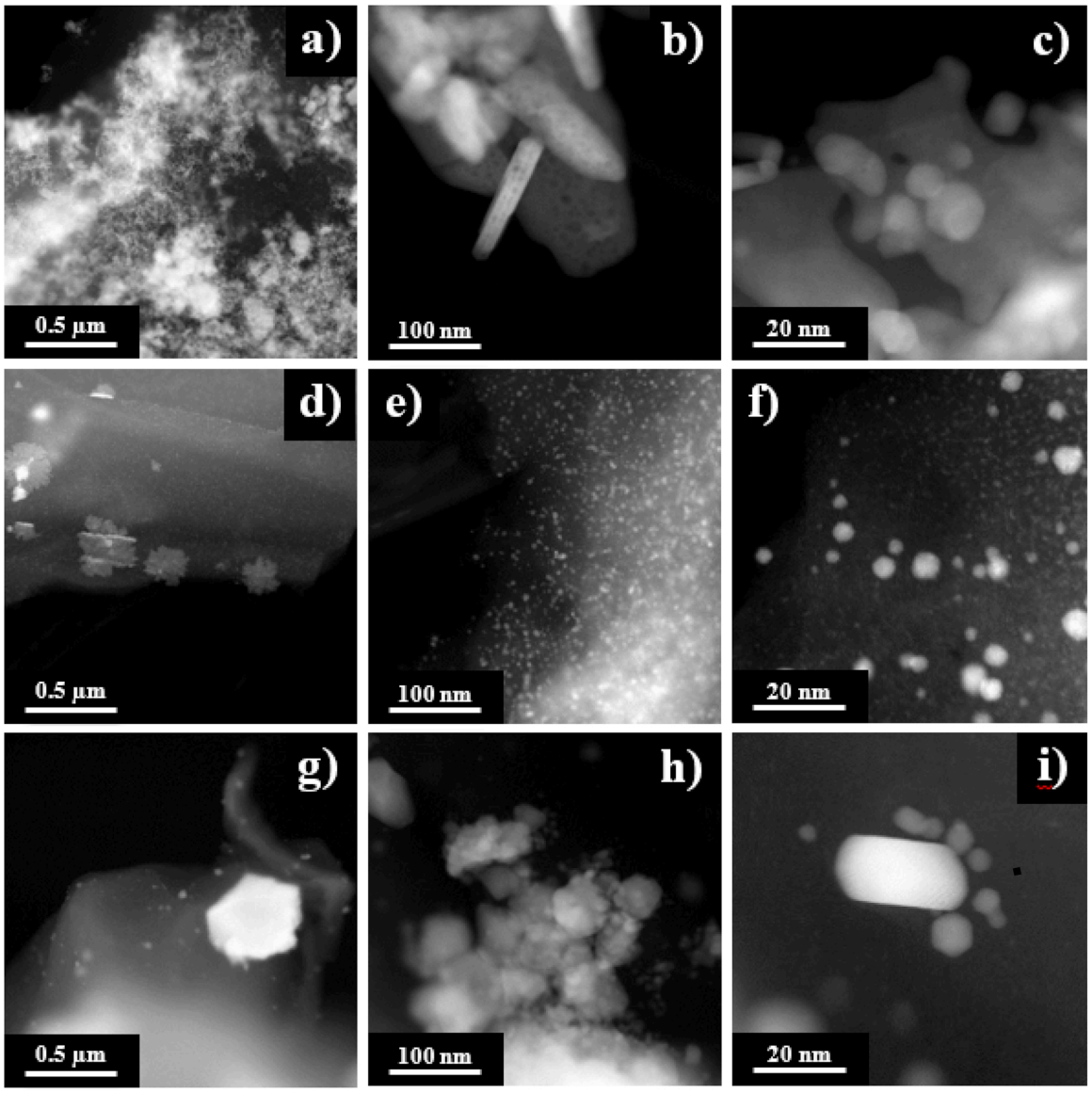

Fig. 7. Z-Contrast dark-field TEM images for GO+Pd (a-c), GO+ODA+Pd (d-f) and GO+DAO+Pd (g-i) at different magnification. Scale bars: 0.5 µm (left column); 100 nm (middle column), and 20 nm (right column).

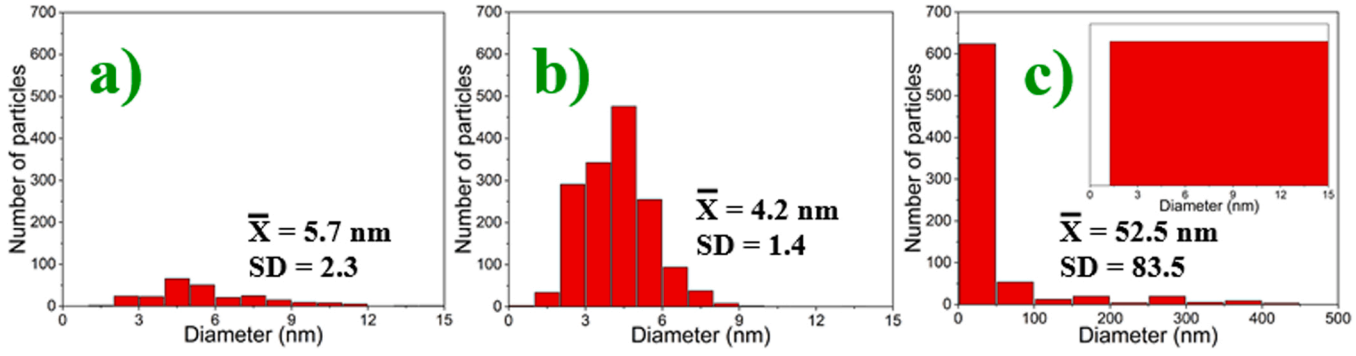

Fig. 8. Particle size distribution histograms obtained from TEM imaging of (a) GO+Pd, (b) GO+ODA+Pd and (c) GO+DAO+Pd. The inset in (c) shows the main population of particles ranging from 1 to 15 nm onwards represented by the maximum on the histogram.

of rather long DAO moieties. This direct contact between the Pd_{16} cluster and the graphene backbone 'smears' palladium atoms over the GO surface, contrary to the case of GO+ODA+Pd_{16}, where Pd_{16} generally conserves its symmetric shape. A possible explanation is that ODA substituents are sufficiently long, and thus 'shield' and protect palladium from the strong attraction to the GO surface. The 'smearing'

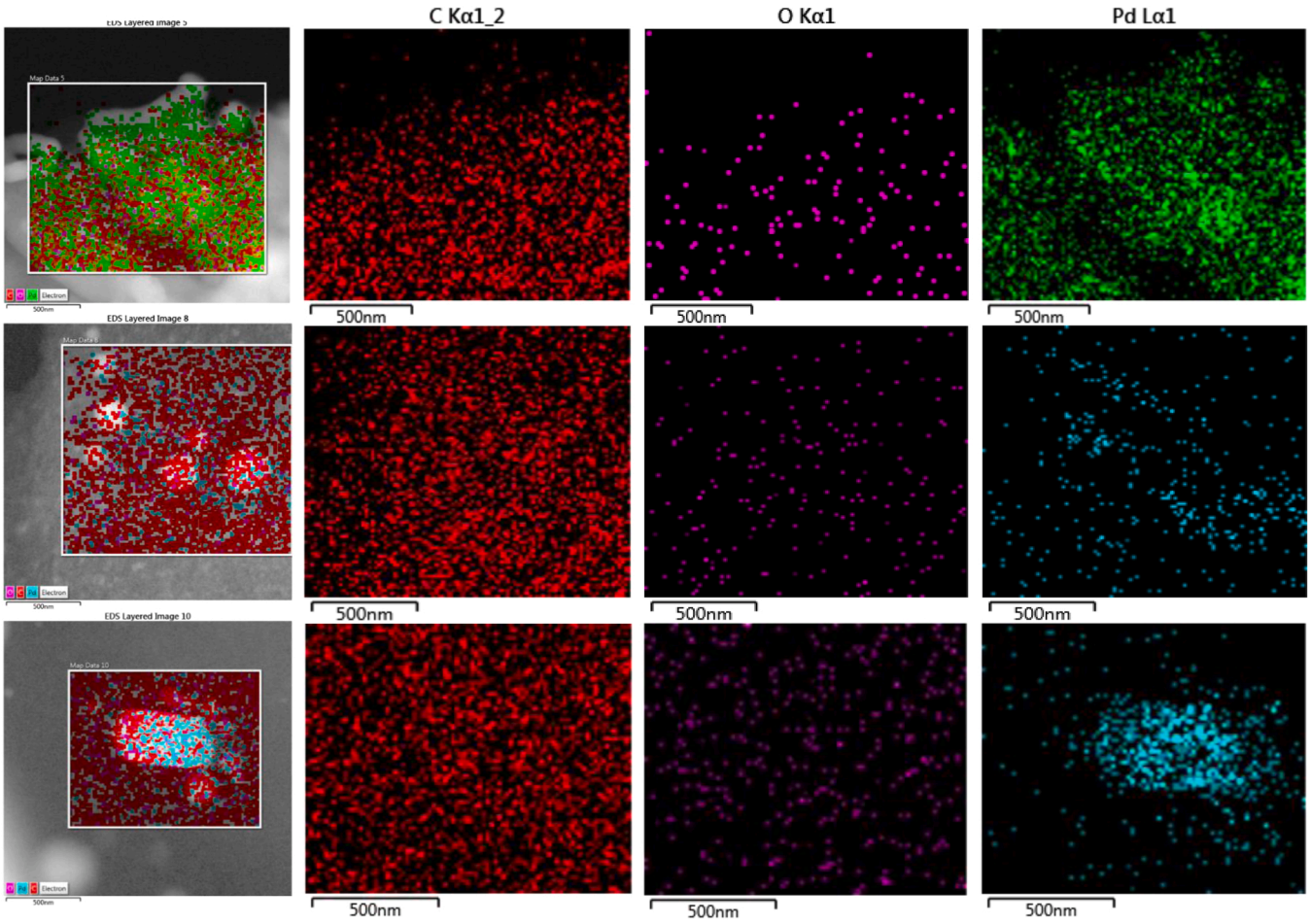

Fig. 9. C, O and Pd elemental mapping and all maps overlaid on the TEM micrograph (left. column) for GO+Pd (top row), GO+ODA+Pd (middle row) and GO+DAO+Pd (bottom row).

Table 2
EDS results for the GO/PdNPs series (TEM imaging).

Sample	Weight %	Atomic %
GO+Pd	C (K): 24.6 ± 7.6	C (K): 69.9 ± 10.1
	O (K): 2.7 ± 1.4	O (K): 6.1 ± 4.0
	Pd (L): 72.7 ± 6.2	Pd (L): 24.1 ± 6.1
GO+ODA+Pd	C (K): 60.0 ± 20.2	C (K): 86.0 ± 8.4
	O (K): 6.9 ± 1.8	O (K): 8.0 ± 3.9
	Pd (L): 33.1 ± 18.5	Pd (L): 6.0 ± 4.5
GO+DAO+Pd	C (K): 46.8 ± 16.8	C (K): 82.1 ± 3.6
	O (K): 6.0 ± 4.8	O (K): 7.3 ± 4.1
	Pd (L): 47.2 ± 21.6	Pd (L): 10.6 ± 7.7

of Pd atoms observed theoretically can explain PdNP coalescence and agglomeration observed experimentally on GO and GO+DAO, whereas PdNPs deposited onto GO+ODA do not tend to coalesce and remain small, though the Pd elemental content is relatively small as well.

As it could be expected, the differences in geometries and mechanisms of nanohybrid formation give rise to notable differences in the electronic structure; we analyzed specifically the energy and distribution of frontier orbitals HOMO and LUMO (Table 3 and Fig. 13). The HOMO-LUMO gap energies calculated for individual components are 0.313 eV for Pd_{16}, 1.105 eV GO, 0.854 eV for GO+ODA and 0.863 eV for GO+DAO-4 H^+ are (Table 3). It is logical to expect that, since Pd_{16} has the lowest gap energy of all these components, its complexation with GO, GO+ODA and GO+DAO-4 H^+ will result in lower HOMO-LUMO gap energies for the corresponding hybrids. As one can see, the HOMO-LUMO gap dramatically decreases to 0.163 eV for GO+Pd_{16}, 0.008 eV for GO+ODA+Pd_{16} and 0.144 eV for GO+DAO-4 H^++Pd_{16}. An especially interesting observation is that Pd functionalization decreases the gap energy by two orders of magnitude, namely from 0.854 eV for GO+ODA to 0.008 eV for GO+ODA+Pd_{16}. The frontier orbital localization (Fig. 13) matches the differences in HOMO-LUMO gap energies. The very strong interaction in the cases of GO+Pd_{16} and GO+DAO-4 H^++Pd_{16} results in the localization of both the HOMO and the LUMO on the same Pd atoms and an insignificant charge density on GO. On the contrary, in GO+ODA+Pd_{16} the HOMO and the LUMO are very well separated, with the HOMO localized exclusively on GO, and the LUMO exclusively on Pd_{16}. The fact that the LUMO in all three cases is centered on Pd might imply that the latter remains active in electrophilic processes; in addition the presence of the HOMO on the same atoms in GO+Pd_{16} and GO+DAO-4 H^++Pd_{16} can be linked to Pd cluster activity in nucleophilic processes. In turn, this might have important positive consequences for catalytic, electrocatalytic and biomedical applications of PdNPs deposited onto GO and GO-based materials. Table 4.

4. Conclusions

Dispersibility tests, FTIR, XRD, TGA/DTA, as well as SEM and TEM imaging accompanied with EDS mapping, gave indications that applying an eco-friendly gas-phase functionalization of GO with amines is useful to create supports for the decoration with Pd nanoparticles. However the palladium content in non-aminated GO+Pd samples is higher than in amine-functionalized GO. XRD results showed Pd (111) and (200) peaks, indicating that the larger palladium nanoparticles, which are

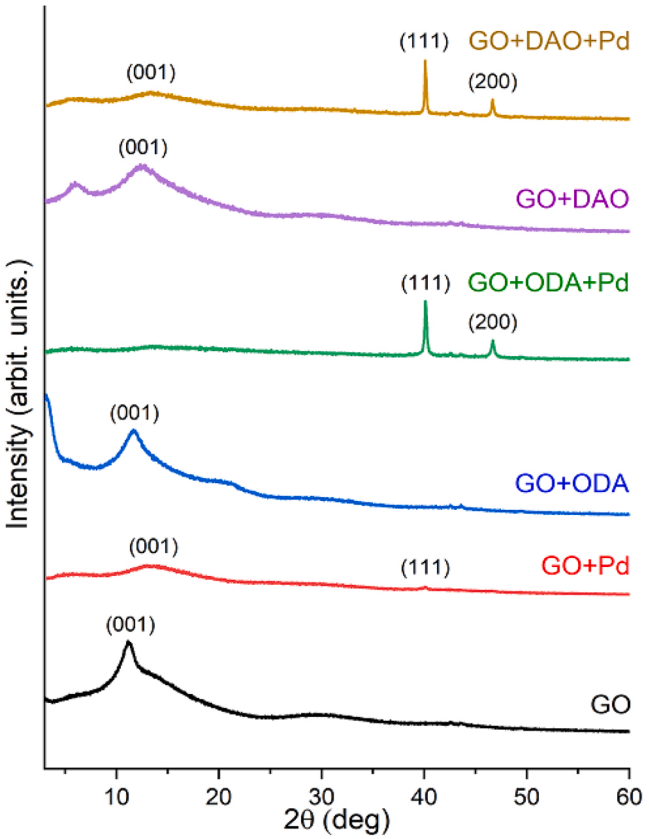

Fig. 10. XRD diffractograms of pristine and amine-functionalized GO before and after decoration with Pd nanoparticles.

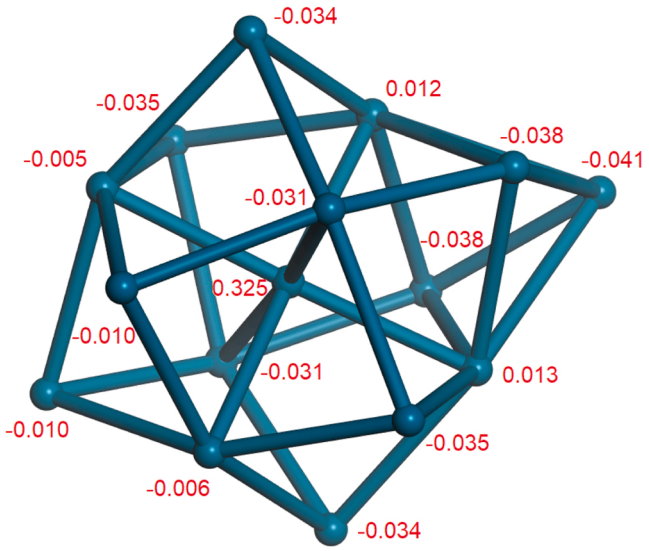

Fig. 11. Optimized geometry of the Pd16 cluster used to simulate PdNPs, showing atomic charges obtained by Mulliken analysis.

Table 3
Particle size distribution for the GO/PdNP series by SEM and TEM imaging.

Sample	Average SEM (μm)	Average TEM (nm)
GO+Pd	0.13 ± 0.05	5.69 ± 2.28
GO+ODA+Pd	0.26 ± 0.23	4.23 ± 1.37
GO+DAO+Pd	0.14 ± 0.12	52.46 ± 83.47

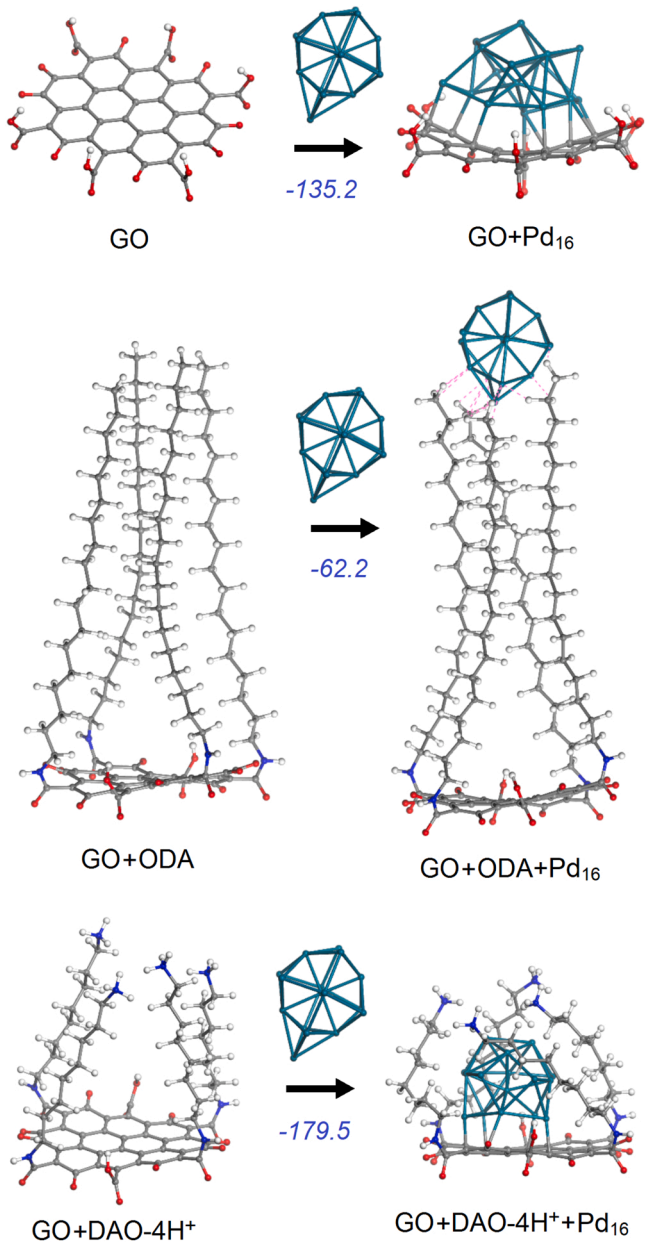

Fig. 12. Optimized geometries of the GO, GO+ODA and GO+DAO-4 H^+ models (left) and of their hybrids formed with a Pd_{16} nanocluster (right) in aqueous medium. The values shown in blue are the formation energies (in kcal/mol) for GO+Pd_{16}, GO+ODA+Pd_{16} and GO+DAO-4 H^++Pd_{16} hybrids. The pink dashed lines indicate closest approaches shorter than 2.8 Å.

visible to this technique, crystallize with a face centered cubic (fcc) structure. Electronic imaging evidence differences in PdNPs nucleation and shape with the amount of stabilizing agents (citric acid, and amine moieties).

The most relevant explanation could be obtained from bright-field and dark-field TEM imaging. GO+Pd samples we found to contain particles that generally are irregularly shaped and randomly distributed, whereas a more homogeneous size distribution preventing agglomeration was observed for ODA-functionalized GO. DAO-functionalized samples presented the formation of particles with different sizes, shapes, and coalescence. The average Pd particle sizes were found to be ten times larger on GO functionalized with diamines than on pristine GO, and on GO with monoamines.

Referring to theoretical data, the fact that the LUMO in all three cases is centred on Pd, might imply that the latter remains active in

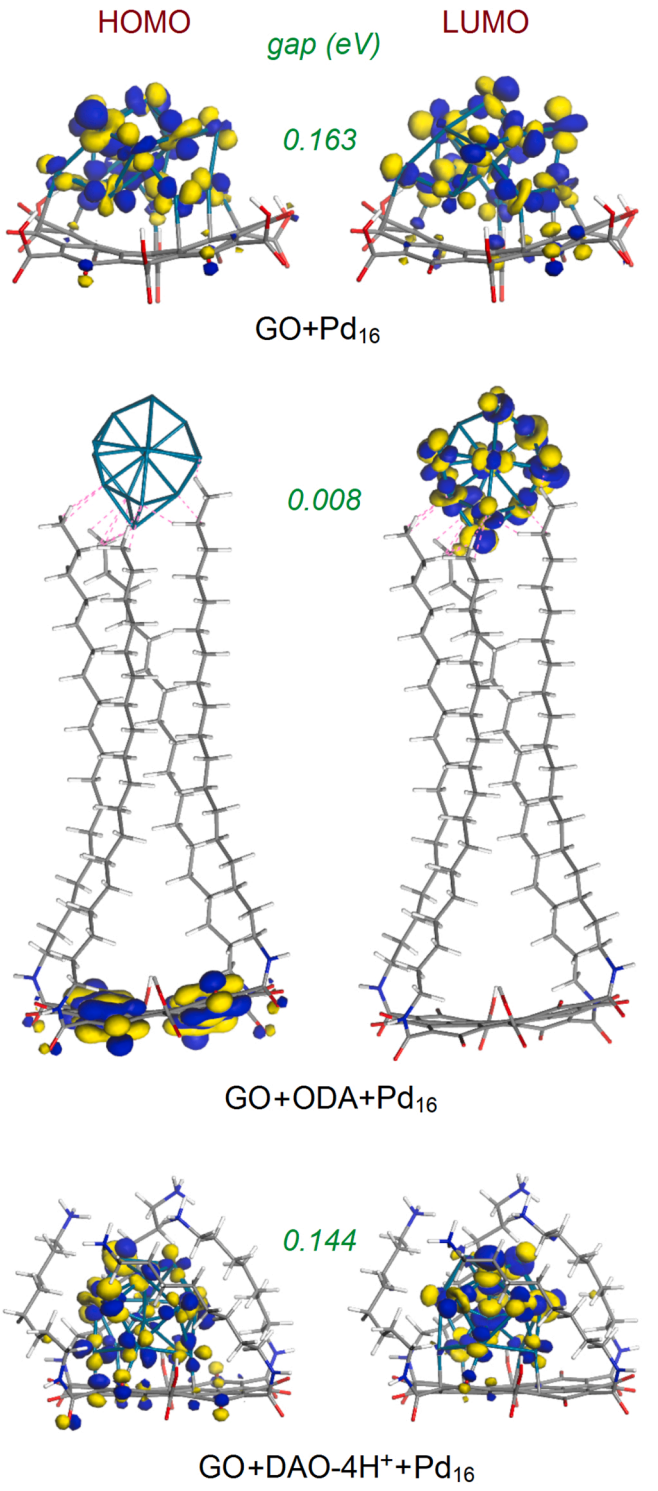

Fig. 13. HOMO and LUMO plots (isosurfaces at 0.03 a.u.) of the GO+Pd_{16}, GO+ODA+Pd_{16} and GO+DAO-4 H^++Pd_{16} hybrids, with the HOMO-LUMO gap values shown in green.

electrophilic processes; in addition the presence of the HOMO on the same atoms in GO+Pd_{16} and GO+DAO-4 H^++Pd_{16} can be linked to Pd cluster activity in nucleophilic processes. In turn, this might have important positive consequences for catalytic, electrocatalytic and biomedical applications of PdNPs deposited onto GO-based materials.

Table 4
Total energies (*E*, in Ha), HOMO, LUMO and HOMO-LUMO gap energies (in eV) for an isolated Pd_{16} cluster, pristine and amine-functionalized GO models and their corresponding complexes with Pd_{16}, as well as formation energies (ΔE, in kcal/mol) for the complexes with Pd_{16}, as calculated by using PBE GGA functional with Grimme's dispersion correction in conjunction with DNP basis set and DSPP pseudopotentials.

Structure	*E* (Ha)	ΔE (kcal/mol)	E_{HOMO} (eV)	E_{LUMO} (eV)	HOMO-LUMO gap (eV)
Pd_{16}	-2613.7569726		-4.533	-4.220	0.313
GO	-2954.3392137		-6.923	-5.818	1.105
GO+Pd_{16}	-5568.3115699	**-135.2**	-5.635	-5.472	0.163
GO+ODA	-5702.6968554		-6.476	-5.622	0.854
GO+ODA+Pd_{16}	-8316.5529615	**-62.2**	-5.037	-5.029	0.008
GO+DAO-4 H^+	-4354.7741375		-6.596	-5.733	0.863
GO+DAO-4 H^++Pd_{16}	-6968.8172249	**-179.5**	-5.763	-5.619	0.144

CRediT authorship contribution statement

Dinorah I. Rodríguez-Otamendi: Conceptualization, Methodology, Validation, Investigation, Visualization, Writing – original draft. **Monserrat Bizarro Sordo**: Investigation, Validation, Visualization. **Victor Meza-Laguna**: Investigation, Validation, Visualization. **Edgar Alvarez-Zauco**: Investigation, Validation, Visualization. **Petra Rudolf**: Validation, Visualization, Supervision, Writing – review & editing. **Vladimir A. Basiuk**: Investigation, Methodology, Validation, Visualization, Writing – review & editing. **Elena V. Basiuk**: Conceptualization, Methodology, Validation, Supervision, Project administration, Funding acquisition, Writing – review & editing.

Declaration of Competing Interest

The authors declare that they have no known competing financial interests or personal relationships that could have appeared to influence the work reported in this paper.

Data Availability

No data was used for the research described in the article.

Acknowledgements

Financial support from the National Autonomous University of Mexico (UNAM; grant DGAPA-IN100821) is greatly appreciated. This work was also supported by the Advanced Materials research program of the Zernike National Research Centre under the Bonus Incentive Scheme (BIS) of the Dutch Ministry for Education, Culture and Science. D. I. R. O., is indebted to the Postgraduate Program in Chemical Sciences at UNAM and the National Council of Science and Technology of Mexico (CONACyT), as well as the Double Degree Program between the UNAM and the University of Goningen for a PhD scholarship. We thank the technical support from the University Spectroscopic Characterization Laboratory (LUCE_ICAT_UNAM) and the technician, Dr. Selene Rubí Islas Sánchez for her assistance in the acquisition of FT-IR spectra. We are also grateful to Dr. Josué Esaú Romero-Ibarra for assistance in the TEM studies.

References

[1] K.S. Kumar, N. Choudhary, Y. Jung, Y. Thomas, Recent advances in two-dimensional nanomaterials for supercapacitor electrode applications, ACS Energy Lett. 3 (2) (2018) 482–495.
[2] G.I. Zhuang, Y.F. Gao, X. Zhou, X.Y. Tao, J.M. Luo, Y.J. Gao, Y.I. Yan, P.Y. Gao, X. Zhong, J.G. Wang, ZIF-67/COF-derived highly dispersed Co_3O_4/N-doped porous carbon with excellent performance for oxygen evolution reaction and Li-ion batteries, Chem. Eng. J. 330 (2017) 1255–1564.

[3] A. Díez-Pascual, J. Luceño Sánchez, R. Peña Capilla, P. García Díaz, Recent developments in graphene/polymer nanocomposites for application in polymer solar cells, Polymers 10 (2) (2018) 1–22.
[4] M. Hu, Z. Yao, X. Wang, Graphene-based nanomaterials for catalysis, Ind. Eng. Chem. Res. 56 (13) (2017) 3477–3502.
[5] D.A. Dikin, S. Stankovich, E.J. Zimney, R.D. Piner, G.H.B. Dommett, G. Evmenenko, S.T. Nguyen, R.S. Ruoff, Preparation and characterization of graphene oxide paper, Nature 448 (2007) 457–460.
[6] C. Vallés, J.D. Núñez, A.M. Benito, W.K. Maser, Flexible conductive graphene paper obtained by direct and gentle annealing of graphene oxide paper, Carbon 50 (2012) 835–844.
[7] Y. Zhang, C. Tai-Shung, Graphene oxide membranes for nanofiltration, Curr. Opin. Chem. Eng. 16 (2017) 9–15.
[8] H. Chen, M.B. Müller, K.J. Gilmore, G.G. Wallace, D. Li, Mechanically strong, electrically conductive, and biocompatible graphene paper, Adv. Mater. 20 (18) (2008) 3557–3561.
[9] W. Huang, Graphene oxide papers, in: W. Huang (Ed.), Nanopapers: From Nanochemistry and Nanomanufacturing to Advanced Applications, 1st ed.,, Elsevier, Amsterdam, 2017, pp. 1–26. Ch. 1.
[10] M. Cobos, I. De-La-Pinta, G. Quindós, M.J. Fernández, M.D. Fernández, Graphene oxide–silver nanoparticle nanohybrids: synthesis, characterization, and antimicrobial properties, Nanomaterials 10 (376) (2020) 1–22.
[11] Y. Cheng, H. Li, C. Fang, L. Ai, J. Chen, J. Su, Q. Zhang, Q. Fu, Facile synthesis of reduced graphene oxide/silver nanoparticles composites and their application for detecting heavy metal ions, J. Alloy. Compd. 787 (2019) 683–693.
[12] M. Ayán-Varela, M.J. Fernández-Merino, J.I. Paredes, S. Villar-Rodil, C. Fernández-Sánchez, L. Guardia, A. Martínez-Alonso, J.M.D. Tascón, Highly efficient silver-assisted reduction of graphene oxide dispersions at room temperature: mechanism, and catalytic and electrochemical performance of the resulting hybrids, J. Mater. Chem. A 2 (20) (2014) 7295–7305.
[13] S. Navalon, A. Dhakshinamoorthy, M. Álvaro, H. Garcia, Metal nanoparticles supported on two-dimensional graphenes as heterogeneous catalysts, Coord. Chem. Rev. 312 (2016) 99–148.
[14] H. Golzar, F. Yazdian, M. Hashemi, M. Omidi, D. Mohammadrezaei, H. Rashedi, M. Farahani, N. Ghasemi, J.S. Shayeh, L. Tayebi, Optimizing the hybrid nanostructure of functionalized reduced graphene oxide/silver for highly efficient cancer nanotherapy, N. J. Chem. 42 (15) (2018) 13157–13168.
[15] N. Cai, J. Fu, H. Zeng, X. Luo, C. Han, F. Yu, Reduced graphene oxide-silver nanoparticles/nitrogen-doped carbon nanofiber composites with mesomicroporous structure for high-performance symmetric supercapacitor application, J. Alloy. Compd. 742 (2018) 769–779.
[16] F. Zeng, D. Xu, C. Zhan, C. Liang, W. Zhao, J. Zhang, H. Feng, X. Ma, Surfactant-free synthesis of graphene oxide coated silver nanoparticles for SERS biosensing and intracellular drug delivery, ACS Appl. Nano Mater. 1 (6) (2018) 2748–2753.
[17] C. Shuai, W. Guo, P. Wu, W. Yang, S. Hu, Y. Xia, P. Feng, A graphene oxide-Ag co-dispersing nanosystem: dual synergistic effects on antibacterial activities and mechanical properties of polymer scaffolds, Chem. Eng. J. 347 (2018) 322–333.
[18] Y. Jiang, D. Carboni, L. Malfatti, P. Innocenzi, Graphene oxide-silver nanoparticles in molecularly-imprinted hybrid films enabling SERS selective sensing, Materials 11 (9) (2018) 1–17, 1674.
[19] A. Kumar, B. Mazinder Boruah, X.-J. Liang, Gold nanoparticles: promising nanomaterials for the diagnosis of cancer and HIV/AIDS, J. Nanomater. (2011) 1–17.
[20] V.K. Sharma, C.M. Sayes, B. Guo, S. Pillai, J.G. Parsons, C. Wang, B. Yan, X. Ma, Interactions between silver nanoparticles and other metal nanoparticles under environmentally relevant conditions: a review, Sci. Total Environ. 653 (2019) 1042–1051.
[21] P.K. Singh, P. Kumar, A. Kumar, Unconventional physical methods for synthesis of metal and non-metal nanoparticles: a review, Proc. Natl. Acad. Sci. India A - Phys. Sci. 89 (2) (2018) 199–221.
[22] D.R. Dreyer, S. Park, C.W. Bielawski, R.S. Ruoff, The chemistry of graphene oxide, Chem. Soc. Rev. 39 (2009) 228–240.
[23] S. Gurunathan, J.H. Park, Y.-J. Choi, J.W. Han, J.-H. Kim, Synthesis of graphene oxide-silver nanoparticle nanocomposites: an efficient novel antibacterial agent, Curr. Nanosci. 12 (6) (2016) 762–773.
[24] Q. Bao, D. Zhang, P. Qi, Synthesis and characterization of silver nanoparticle and graphene oxide nanosheet composites as a bactericidal agent for water disinfection, J. Colloid Interface Sci. 360 (2) (2011) 463–470.
[25] Z. Li, J. Gao, X. Xing, S. Wu, S. Shuang, C. Dong, M.C. Paau, M.M.F. Choi, Synthesis and characterization of n-alkylamine-stabilized palladium nanoparticles for electrochemical oxidation of methane, J. Phys. Chem. C 114 (2) (2010) 723–733.
[26] A.M. Dimiev, S. Eigler (Eds.), Graphene Oxide: Fundamentals and Applications, Wiley, Chichester, 2017.
[27] J. Li, D. Kuang, Y. Feng, F. Zhang, Z. Xu, M. Liu, D. Wang, Green synthesis of silver nanoparticles–graphene oxide nanocomposite and its application in electrochemical sensing of tryptophan, Biosens. Bioelectron. 42 (2013) 198–206.
[28] D.I. Rodríguez-Otamendi, V. Meza-Laguna, D. Acosta, E. Alvarez-Zauco, L. Huerta, V.A. Basiuk, E.V. Basiuk, Eco-friendly synthesis of graphene oxide–silver nanoparticles hybrids: The effect of amine derivatization, Diam. Relat. Mater. 111 (2021) 1–21.
[29] S. Kumari, P. Sharma, S. Yadav, J. Kumar, A. Vij, P. Rawat, S. Kumar, C. Sinha, J. Bhattacharya, C. Mohan Srivastava, S. Majumder, A novel synthesis of the graphene oxide-silver (GO-Ag) nanocomposite for unique physiochemical applications, ACS Omega 5 (10) (2020) 5041–5047.
[30] T.T.T. Vi and S.J. Lue, Preparation of silver nanoparticles loaded graphene oxide nanosheets for antibacterial activity, IOP Conf. Ser.: Mater. Sci. Eng. 162 (2016) 012033 (1–5).
[31] H.-S. Kim, H. Lee, K.-S. Han, J.-H. Kim, M.-S. Song, M.-S. Park, J.-Y. Lee, J.-K. Kang, Hydrogen storage in Ni nanoparticle-dispersed multiwalled carbon nanotubes, J. Phys. Chem. B 109 (18) (2005) 8983–8986.
[32] L.-M. Ang, T.S. Andy Hor, G.-Q. Xu, C. Tung, S. Zhao, J.L. Wang, Electroless plating of metals onto carbon nanotubes activated by a single-step activation method, Chem. Mater. 11 (8) (1999) 2115–2118.
[33] P.S. Karthik, A.L. Himaja, S.P. Singh, Carbon-allotropes: synthesis methods, applications and future perspectives, Carbon Lett. 15 (4) (2014) 219–237.
[34] D. Zhang, T. Liu, J. Cheng, S. Liang, J. Chai, X. Yang, H. Wang, G. Zheng, M. Cao, Controllable synthesis and characterization of tungsten disulfide nanosheets as promising nanomaterials for electronic devices, Ceram. Int. 45 (9) (2019) 12443–12448.
[35] V.R. Bakuru, B. Velaga, N.R. Peela, S.B. Kalidindi, Hybridization of Pd nanoparticles with UiO-66(Hf) metal-organic framework and the effect of nanostructure on the catalytic properties, Chem. A Eur. J. 24 (60) (2018) 15978–15982.
[36] D.K. Pattadar, J.N. Sharma, B.P. Mainali, F.P. Zamborini, Anodic stripping electrochemical analysis of metal nanoparticles, Curr. Opin. Electrochem 13 (2019) 147–156.
[37] S.B. Yaqoob, R. Adnan, R.M. Rameez Khan, M. Rashid, Gold, silver, and palladium nanoparticles: a chemical tool for biomedical applications, Front. Chem. 8 (376) (2020) 1–15.
[38] C.P. Adams, K.A. Walker, S.O. Obare, K.M. Docherty, Size-dependent antimicrobial effects of novel palladium nanoparticles, PLoS ONE 9 (2014) 85–98.
[39] K. Chaloupka, Y. Malam, A.M. Seifalian, Nanosilver as a new generation of nanoproduct in biomedical applications, Trend Biotechnol. 28 (11) (2010) 580–588.
[40] V. Leso, I. Iavicoli, Palladium nanoparticles: toxicological effects and potential implications for occupational risk assessment, Int. J. Mol. Sci. 19 (2018) 503.
[41] J. Bandekar, Amide modes and protein conformation, Biochim Biophys. Acta 1120 (2) (1992) 123–143.
[42] N. Alzate-Carvajal, E.V. Basiuk, V. Meza-Laguna, I. Puente-Lee, M.H. Farias, N. Bogdanchikova, V.A. Basiuk, Solvent-free one-step covalent functionalization of graphene oxide and nanodiamond with amines, RSC Adv. 6 (2016) 113596–113610.
[43] N. Alzate-Carvajal, D.A. Acevedo-Guzmán, V. Meza-Laguna, M.H. Farías, L. A. Pérez-Rey, E. Abarca-Morales, V.A. García-Ramírez, V.A. Basiuk, E.V. Basiuk, One-step nondestructive functionalization of graphene oxide paper with amines, RSC Adv. 8 (2018) 15253–15265.
[44] E.V. Basiuk, V.A. Basiuk, V. Meza-Laguna, F.F. Contreras-Torres, M. Martínez, A. Rojas-Aguilar, M. Salerno, G. Zavala, A. Falqui, R. Brescia, Solvent-free covalent functionalization of multi-walled carbon nanotubes and nanodiamond with diamines: looking for cross-linking effects, Appl. Surf. Sci. 259 (2012) 465–476.
[45] P.S. Roy, J. Bagchi, S.K. Bhattacharya, Size-controlled synthesis and characterization of polyvinyl alcohol coated palladium nanoparticles, Transit. Met. Chem. 34 (4) (2009) 447–453.
[46] R.A. Dar, L. Giri, S.P. Karna, A.K. Srivastava, Performance of palladium nanoparticle–graphene composite as an efficient electrode material for electrochemical double layer capacitors, Electrochim. Acta 196 (2016) 547–557.
[47] J. Li, W. Chen, H. Zhao, X. Zheng, L. Wu, H. Pan, J. Zhu, Y. Chen, J. Lu, Size-dependent catalytic activity over carbon-supported palladium nanoparticles in dehydrogenation of formic acid, J. Catal. 352 (2017) 371–381.
[48] B. Delley, An all-electron numerical method for solving the local density functional for polyatomic molecules, J. Chem. Phys. 92 (1990) 508–517.
[49] B. Delley, Fast calculations of electrostatics in crystals and large molecules, J. Phys. Chem. 100 (1996) 6107–6110.
[50] B. Delley, From molecules to solids with the DMol3 approach, J. Chem. Phys. 113 (2000) 7756–7764.
[51] B. Delley, D.E. Ellis, A.J. Freeman, E.J. Baerends, D. Post, Binding energy and electronic structure of small copper particles, Phys. Rev. B 27 (1983) 2132–2144.
[52] J.P. Perdew, K. Burke, M. Ernzerhof, Generalized gradient approximation made simple, Phys. Rev. Lett. 77 (1996) 3865–3868.
[53] S. Grimme, Semiempirical GGA-type density functional constructed with a long-range dispersion correction, J. Comput. Chem. 27 (2006) 1787–1799.
[54] E.V. Basiuk, L. Huerta, V.A. Basiuk, Noncovalent bonding of *3d* metal(II) phthalocyanines with single-walled carbon nanotubes: a combined DFT and XPS study, Appl. Surf. Sci. 470 (2019) 622–630.
[55] V.A. Basiuk, Electron smearing DFT Calc.: A case Study doxorubicin Interact. Single-walled Carbon Nanotub. 111 (2011) 4197–4205.
[56] V.A. Basiuk, O.V. Prezhdo, E.V. Basiuk, Thermal smearing in DFT calculations: how small is really small? A case of La and Lu atoms adsorbed on graphene, Mater. Today Commun. 25 (2020), 101595.
[57] A. Klamt, G. Schüürmann, COSMO: a new approach to dielectric screening in solvents with explicit expressions for the screening energy and its gradient, Soc. Perkin Trans. 2 (1993) 799–805.
[58] B. Delley, The conductor-like screening model for polymers and surfaces, Mol. Simul. 32 (2006) 117–123.
[59] B.T. McGrail, B.J. Rodier, E. Pentzer, Rapid functionalization of graphene oxide in water, Chem. Mater. 26 (2014) 5806–5811.
[60] R. Yuan, J. Yuan, Y. Wu, L. Chen, H. Zhou, J. Chen, Efficient synthesis of graphene oxide and the mechanisms of oxidation and exfoliation, Appl. Surf. Sci. 416 (2017) 868–877.

[61] A. Barth, Infrared spectroscopy of proteins, Biochim. Biophys. Acta 2007 (1767) 1073–1101.
[62] J. Kong, S. Yu, Fourier transform infrared spectroscopic analysis of protein secondary structures, Acta Biochim. Biophys. Sin. 39 (2007) 549–559.
[63] K. Spyrou, P. Rudolf, An Introduction to Graphene, in Functionalization of Graphene, ed. V. Georgakilas, Wiley-VCH Verlag GmbH & Co. KGaA, Weinheim, 1st ed, 2014, Ch. 1, pp. 1–20.
[64] P.-W. Yen, T.-C. Chou, Temperature programmed oxidation of palladium catalyst: effect of support on the oxygen adsorption behavior, Appl. Catal. A-Gen. 198 (2000) 23–31.
[65] X. Liu, X. Zhao, M. Zhou, Y. Cao, H. Wu, J. Zhu, Highly Stable and Active Palladium Nanoparticles Supported on a Mesoporous UiO66@reduced Graphene Oxide Complex for Practical Catalytic Applications, Eur. J. Inorg. Chem. (2016) 3338–3343.
[66] T. Premkumar, K. Lee, K.E. Geckeler, Shape-tailoring and catalytic function of anisotropic gold nanostructures, Nanoscale Res Lett. 6 (547) (2011) 1–12.
[67] E. Ramirez, S. Jansat, K. Philippot, P. Lecante, M. Gomez, A.M. Masdeu-Bultó, B. Chaudret, Influence of organic ligands on the stabilization of palladium nanoparticles, J. Organomet. Chem. 689 (2004) 4601–4610.
[68] J. Chen, B. Yao, C. Li, G. Shi, An improved Hummers method for eco-friendly synthesis of graphene oxide, Carbon 64 (2013) 225–229.
[69] J. Chen, Y. Li, L. Huang, C. Li, G. Shi, High-yield preparation of graphene oxide from small graphite flakes via an improved Hummers method with a simple purification process, Carbon 81 (2015) 826–834.
[70] C. Wang, Z. Liu, S. Wang, Y. Zhang, Preparation and properties of octadecylamine modified graphene oxide/styrene-butadiene rubber composites through an improved melt compounding method, J. Appl. Polym. Sci. 133 (2016) 42907.
[71] W. Gao, The Chemistry of Graphene Oxide, in: W. Gao (Ed.), Graphene Oxide: Reduction Recipes, Spectroscopy, and Applications, Springer, Cham, Switzerland, 2015, pp. 61–95.
[72] I. Dékány, R. Krüger-Grasser, A. Weiss, Selective liquid sorption properties of hydrophobized graphite oxide nanostructures, Colloid Polym. Sci. 276 (7) (1998) 570–576.
[73] A. Kaniyoor, T.T. Baby, T. Arockiadoss, N. Rajalakshmi, S. Ramaprabhu, Wrinkled graphenes: a study on the effects of synthesis parameters on exfoliation-reduction of graphite oxide, J. Phys. Chem. C. 115 (2011) 17660–17669.
[74] N. Díez, A. Sliwak, S. Gryglewicz, B. Grzyb, G. Gryglewicz, Enhanced reduction of graphene oxide by high-pressure hydrothermal treatment, RSC Adv. 5 (2015) 81831.
[75] S. Choudhary, H.P. Mungse, O.P. Khatri, Dispersion of alkylated graphene in organic solvents and its potential for lubrication applications, J. Mater. Chem. 22 (2012) 21032–21039.
[76] H.P. Mungse, O.P. Khatri, Chemically functionalized reduced graphene oxide as a novel material for reduction of friction and wear, J. Phys. Chem. C. 118 (2014) 14394–14402.
[77] G. Wang, J. Yang, J. Park, X. Gou, B. Wang, H. Liu, J. Yao, Facile synthesis and characterization of graphene nanosheets, J. Phys. Chem. C. 112 (2008) 8192–8195.
[78] W.-S. Hung, C.-H. Tsou, M. De Guzman, Q.-F. An, Y.-L. Liu, Y.-M. Zhang, C.-C. Hu, K.-R. Lee, J.-Y. Lai, Cross-linking with diamine monomers to prepare composite graphene oxide-framework membranes with varying *d-Spacing*, Chem. Mater. 26 (9) (2014) 2983–2990.
[79] R. Molaei, K. Farhadi, M. Forough, S. Hajizadeh, Green biological fabrication and characterization of highly monodisperse palladium nanoparticles using pistacia atlantica fruit broth, J. Nanostruct. 8 (1) (2018) 47–54.
[80] P. Nava, M. Sierka, R. Ahlrichs, Density functional study of palladium clusters, Phys. Chem. Chem. Phys. 5 (2003) 3372–3381.
[81] N.T. Tran, M. Kawano, L.F. Dahl, High-nuclearity palladium carbonyl trimethylphosphine clusters containing unprecedented face-condensed icosahedral-based transition-metal core geometries: proposed growth patterns from a centered Pd_{13} icosahedron, J. Chem. Soc. Dalton Trans. 19 (2001) 2731–2748.
[82] V.A. Basiuk, N. Alzate-Carvajal, L.V. Henao-Holguín, E.V. Rybak-Akimova, E. V. Basiuk, Coordination functionalization of graphene oxide with tetraazamacrocyclic complexes of nickel(II): generation of paramagnetic centers, Appl. Surf. Sci. 371 (2016) 16–27.
[83] V.A. Basiuk, E.V. Rybak-Akimova, E.V. Basiuk, Graphene oxide and nanodiamond: Same carboxylic groups, different complexation properties, RSC Adv. 7 (2017) 17442–17450.